**RESEARCH**                                                                 **Open Access**

# Channel characteristics of MIMO–WLAN communications at 60 GHz for various corridors

Shu-Han Liao[1], Chien-Ching Chiu[1*], Chien-Hung Chen[2] and Min-Hui Ho[1]

## Abstract

A comparison of $4 \times 4$ multiple-input multiple-output wireless local area network wireless communication characteristics for six different geometrical shapes is investigated. These six shapes include the straight shape corridor with rectangular cross section, the straight shape corridor with arched cross section, the curved shape corridor with rectangular cross section, the curved shape corridor with arched cross section, the L-shape corridor, and the T-shape corridor. The impulse responses of these corridors are computed by applying shooting and bouncing ray/image (SBR/Image) techniques along with inverse Fourier transform. By using the impulse response of these multipath channels, the mean excess delay, root mean square (RMS) delay spread for these six corridors can be obtained. Numerical results show that the capacity for the rectangular cross section corridors is smaller than those for the arched cross section corridors regardless of the shapes. And the RMS delay spreads for the T-and the L-shape corridors are greater than the other corridors.

**Keywords:** MIMO–WLAN, Corridors, SBR/image, Mean excess delay, RMS delay spread

## 1. Introduction

In recent years, there has been a growing interest in the development of potentially mass-producible wireless systems using millimeter waves, such as wireless local area networks (WLAN) systems [1]. To develop millimeter-wave wireless LAN systems, however, we need to know the reflection and transmission characteristics in millimeter-wave bands so that we can evaluate indoor multipath propagation characteristics and the interactions of millimeter waves with various objects. Many propagation characteristics have extensively been studied, and several models have focused on specific indoor environments [2,3]. Lee and Bertoni [4] use a hybrid ray-mode conversion model for the L-bend and T-junction, respectively, for a 900-MHz signal in a 4-m wide tunnel.

Channel capacity of multiple-input multiple-output (MIMO) for wireless communications in a rich multipath environment is larger than that offered by conventional techniques [5-9]. Channel capacity of WLAN transmission or MIMO transmission has been discussed separately in many literatures. However, there are only few papers dealing with channel capacity of MIMO–WLAN transmission. In [10], the feasibility of dual-polarized antennas in the MIMO system has been validated for indoor scenarios.

This article addresses basic issues regarding the wireless LAN systems that operate in the 60-GHz band as part of the fourth-generation (4G) system [11]. The 60-GHz band provides 7 GHz of unlicensed spectrum with a potential to develop wireless communication systems with multi Gbps throughput. The IEEE 802.11 standard committee [12], one of the major organizations in WLAN specifications development, established the IEEE 802.11ad task group to develop an amendment for the 60-GHz WLAN systems.

All wireless systems must be able to operate in a multipath propagation channel, where object in the environment can cause multiple reflections to arrive at the receiver. In general, effective antenna selection and deployment strategies are important for reducing bit error rate in indoor wireless systems [13,14]. In general, the transmission quality is estimated with strength of power in the narrowband communication system. Besides, a prior knowledge of the characteristics of the channel is necessary for understanding how the signal is affected in the environment. Therefore, many techniques of channel calculation have been developed in recent years. Especially,

---

\* Correspondence: chiu@ee.tku.edu.tw
[1]Department of Electrical Engineering, Tamkang University, Tamsui Dist, New Taipei City, Taiwan
Full list of author information is available at the end of the article

using ray-tracing method to obtain impulse response is extensively applied [15-17]. The different values of dielectric constant and conductivity of materials for different frequencies are carefully considered in channel calculation.

The remainder of this article is organized as follows. In Section 2, system description and channel modeling are presented. Several numerical results are included in Section 3. Section 4 gives the conclusion.

## 2. System description

### 2.1. Channel modeling

The two steps described in the following two subsections are used to calculate the multipath radio channel.

### 2.1.1. Frequency responses for sinusoidal waves by SBR/image techniques

The SBR/image method can deal with high-frequency radio wave propagation in the complex indoor environment [18,19]. It conceptually assumes that many triangular ray tubes are shot from the transmitting antenna (TX), and each ray tube, bouncing, and penetrating in the environment is traced in the indoor multipath channel. If the receiving antenna (RX) is within a ray tube, the ray tube will have contributions to the received field at the RX, and the corresponding equivalent source (image) can be determined. By summing all contributions of these images, we can obtain the total received field at the RX. In real environment, external noise in the channel propagation has been considered. The depolarization yielded by multiple reflections, refraction, and first-order diffraction are also taken into account in our simulations. Note that the different values of dielectric constant and conductivity of materials for different frequencies are carefully considered in channel modeling.

A ray-tracing technique is a good technique to calculate channel frequency response for wireless communication [20-25]. As a result, we develop a ray-tracing technique to model channel for our simulations. Using ray-tracing techniques to predict channel characteristic is effective and fast [18,19,26]. Thus, a ray-tracing channel model is developed to calculate the channel matrix of WLAN system. Flow chart of the ray-tracing process is shown in Figure 1. It conceptually assumes that many triangular ray tubes (not rays) are shot from a transmitter. Here, the triangular ray tubes whose vertexes are on a sphere are determined by the following method. First, we construct an icosahedron which is made of 20 identical equilateral triangles. Then, each triangle of the icosahedron is tessellated into a lot of smaller equilateral triangles. Finally, these small triangles are projected on to the sphere and each ray tube whose vertexes are determined by the small equilateral triangle is constructed [27].

For each ray tube bouncing and penetrating in the environments, we check whether reflection times and penetration times of the ray tube are larger than the numbers of maximum reflection $N_{\mathrm{ref}}$ and maximum penetration $N_{\mathrm{pen}}$, respectively. If it is no, we check whether the receiver falls within the reflected ray tube. If it is yes, the contribution of the ray tube to the receiver can be attributed to an equivalent source (i.e., image source). In other words, a specular ray going to receiver exists in this tube and this ray can be thought as launched from an image source. Moreover, the field diffracted from illuminated wedges of the objects in the environment is calculated by a uniform theory of diffraction [28]. Note that only first diffraction is considered in this article, because the contribution of second diffraction is very small in the analysis. As a result, the corresponding equivalent source (image) can be determined. Some details can refer to literature [29]. By using these images and received fields, the channel frequency response can be obtained as follows:

$$H(f) = \sum_{p=1}^{N_p} a_p(f) e^{j\theta_p(f)}, \tag{1}$$

where $p$ is the path index, $N_p$ is the total number of paths, $f$ is the frequency of sinusoidal wave, $\theta_p(f)$ is the $p$th phase shift, and $\alpha_p(f)$ is the $p$th receiving magnitude. Note that the transmitting and receiving antenna are modeled as a WLAN antenna with simple omnidirectional radiation pattern and vertically polarized. The channel frequency response of WLAN can be calculated from Equation (1) in the frequency range of WLAN.

### 2.1.2. Inverse fast Fourier transform and hermitian processing

The frequency response is transformed to the time domain by using the inverse fast Fourier transform (IFFT) with the Hermitian signal processing [30]. By using the Hermitian processing, the pass-band signal is obtained with zero padding from the lowest frequency down to direct current (DC), taking the conjugate of the signal, and reflecting it to the negative frequencies. The result is then transformed to the time domain using IFFT [31]. Since the signal spectrum is symmetric around DC. The resulting doubled-side spectrum corresponds to a real signal in the time domain.

Using ray-tracing approaches to predict channel characteristic is effective and fast, and the approaches are also usually applied to MIMO channel modeling in recent years [26,32]. Thus, a ray-tracing technique is developed to calculate the channel matrix of MIMO system in this article.

### 2.2. System description

The received signal for a time-invariant narrowband system combining with MIMO (MIMO-NB system) is described as follows [33]:
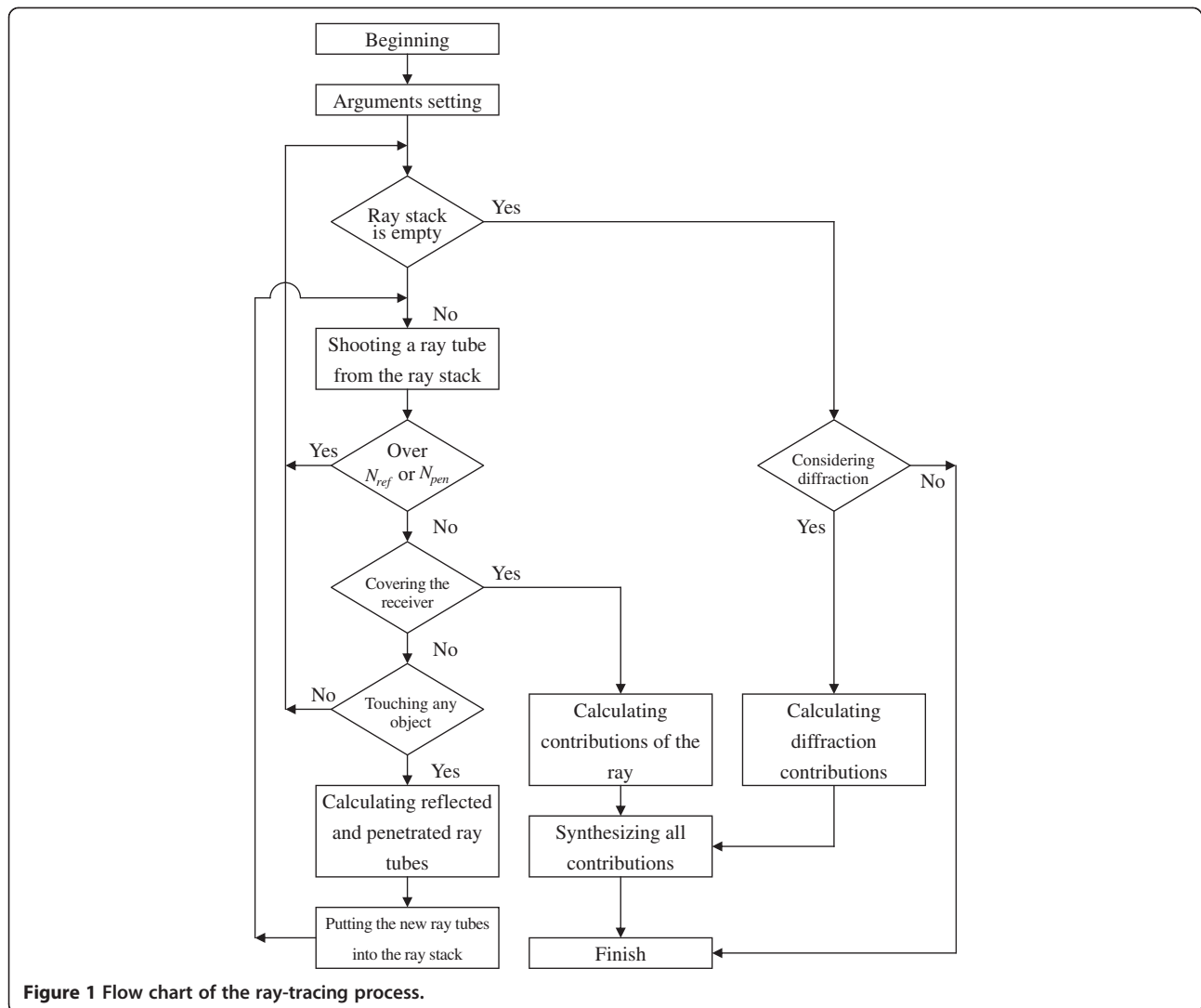
**Figure 1 Flow chart of the ray-tracing process.**

$$\mathbf{Y} = \mathbf{HX} + \mathbf{W} \tag{2}$$

$$H = \begin{bmatrix} h_{11} & h_{12} & h_{13} & \dots & h_{1N_t} \\ h_{21} & h_{22} & h_{33} & \dots & h_{2N_t} \\ h_{21} & h_{22} & h_{33} & \dots & h_{3N_t} \\ \vdots & \vdots & \vdots & \ddots & \vdots \\ h_{N_r1} & h_{N_r2} & h_{N_r3} & \dots & h_{N_rN_t} \end{bmatrix} \tag{3}$$

where $\mathbf{X}$, $\mathbf{Y}$, and $\mathbf{W}$ denote the $N_t \times 1$ transmitted signal vector, the $N_r \times 1$ received signal vector, and the $N_r \times 1$ zero mean additive white Gaussian noise vector at a symbol time, respectively, $\mathbf{H}$ is the $N_r \times N_t$ channel matrix and $h_{ij}$ is the complex channel gain from the $j$th transmitting antenna to the $i$th receiving antenna.

From linear algebra theory, every linear transformation can be represented as a composition of three operations: a rotation operation, a scaling operation, and another rotation operation [28]. As a result, the channel matrix $H$ can be expressed by singular value decomposition as follows

$$\mathbf{H} = \mathbf{UDV}^*, \tag{4}$$

where $\mathbf{U}$ and $\mathbf{V^*}$ are the $N_r \times N_r$ and $N_t \times N_t$ unitary matrices, $\mathbf{D}$ is a $N_r \times N_t$ rectangular matrix whose diagonal elements are non-negative real values and other elements are zero and the symbol * in Equation (4) stands for the conjugate transpose or *Hermitian operation*.

MIMO is capable of signal processing at the transmitter and receiver to produce the set of received signals with highest overall capacity. A matrix representation of MIMO-NB system is shown in Figure 2. In this figure, a linear signal processing operation $V$ is multiplied by the transmitted signal vector $\mathbf{X}$ to produce a new set of signals. The new set of signals is fed further into the MIMO channel. Finally, another linear signal processing

**Figure 2 A matrix representation of MIMO-NB system.**
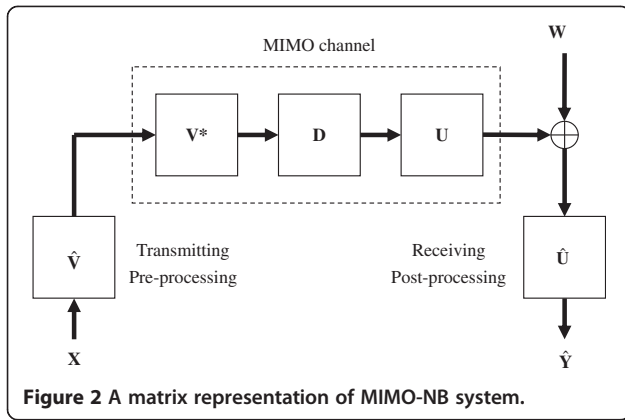
operation $U$ is multiplied by the incoming signal propagating through the channel. The final output signal vector $Y$ is expressed as follows:

$$\hat{Y} = \hat{U}(\mathbf{UDV^*})\hat{V}X + \hat{U}W \quad (5)$$

Note that there is no adding or subtracting of any signal power in the system, because $\hat{V}$ and $\hat{U}$ are both unitary matrices.

If channel state information (CSI) is known for receiver, the channel capacity of the MIMO-NB system can be written in an equivalent matrix notation for $N_t \geq N_r$ as follows [34-36]:

$$C^{\mathrm{NB}} = B\log_2\left(\det\left(I + \frac{\mathrm{SNR}_t}{N_t}HH^*\right)\right), \quad (6)$$

where **I** is an appropriately sized identity matrix. $\mathrm{SNR}_t$ is the ratio of total transmitting power to noise power. $N_t$ is the number of transmitting antennas. $B$ is the bandwidth of the narrowband channel and the symbol * in Equation (6) stands for the conjugate transpose. The equation is especially effective to calculate MIMO capacity in a mathematical software package, since the channel capacity needs CSI for the receiver only.

By the ray-tracing technique, all the frequency responses inside the bandwidth of WLAN between any transmitter and receiver antennas are calculated. Then, MIMO channel capacity of WLAN transmission can be calculated as summation of many channel capacities of narrowband at each discrete frequency point. Thus, the channel capacity (bandwidth efficiency) can be written as follows:

$$C^{\mathrm{WLAN}} = \frac{1}{\mathrm{BW}}\sum_{k=1}^{N_f} C_k^{\mathrm{narrowband}}(\mathrm{bits}/s/\mathrm{Hz}), \quad (7)$$

where BW is the total bandwidth of WLAN and $N_f$ are the numbers of frequency components.

Total channel power gain of MIMO can be defined as follows:

$$P_H = \|\mathbf{H}\|_F^2 = Tr\{\mathbf{R_H}\} = \sum_{k=1}^{N_m}\lambda_k \quad (8)$$

where $\|\cdot\|_F$ denotes the matrix Frobenius norm, $Tr\{\cdot\}$ denotes the matrix trace, and $\lambda_k$ are the eigenvalues of the eigenmatrix $\mathbf{R_H}$. Eigenmatrix can provide information about the relative strengths of the independent transmission modes supported by the MIMO. It is well known that high spatial correlation between sub-channels can reduce the number of significant eigenvalues of eigenmatrix. In other words, just one significant eigenvalue exists with perfect correlation between sub-channels, and $N_m$ significant eigenvalues exist with perfect independence between sub-channels. As a result, the number of significant eigenvalues determines the spatial degrees of freedom and the corresponding channel capacity.
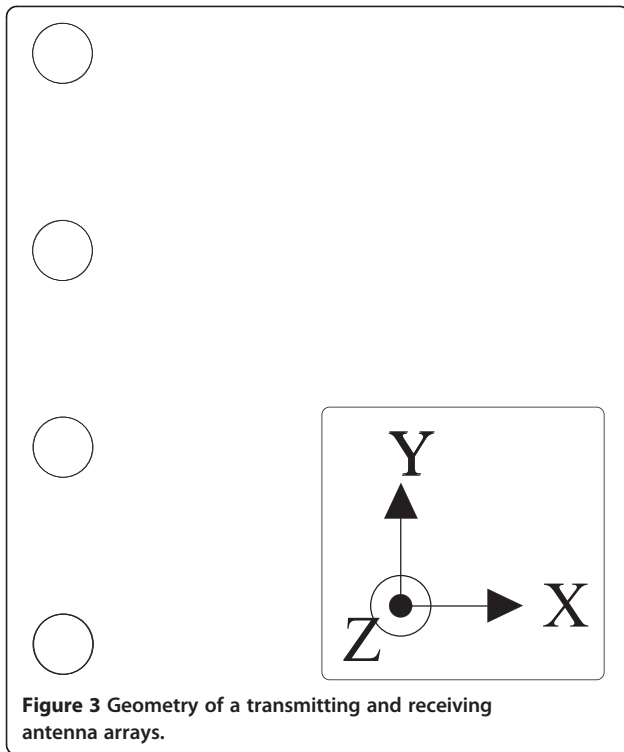
Condition number is an important parameter to decide whether a channel is suitable for MIMO communication, and it can be defined as follows:

$$\mathrm{CN} = \frac{\max\left(\vec{\lambda}_k\right)}{\min\left(\vec{\lambda}_k\right)}; \vec{\lambda}_k = \{\lambda_1, \lambda_2, \lambda_3, \ldots, \lambda_{N_m}\}, \quad (9)$$

where $\vec{\lambda}_k$ is the eigenvalue vector. If total transmitting power is spread equally between all the transmitting antennas, then a system that has highest channel capacity is the one with all the singular values equal. In other words, the eigenvalues are identically equal to $P_H/N_m$, a uniform power allocation strategy optimizes the channel capacity of MIMO-NB system. Furthermore, a channel matrix is said to be well conditioned if its condition number is close to 1, and the elements of the vector $\vec{\lambda}_k$, here are close to each other. As a result, a well-conditional channel matrix can facilitate communication.

## 3. Numerical results

Simulation scenarios and numerical results are presented in this section. A comparison of $4 \times 4$ MIMO WLAN wireless communication characteristics for six different geometrical shapes is investigated. The space between adjacent antennas is 0.0025 m for each antenna array, which satisfies space $(d = \lambda/2)$ without interference between adjacent antennas. Note that the wavelength $\lambda$ is 0.005 m in our simulation. Furthermore, the transmitting and receiving antennas in these six different corridors are both linear array, as shown in Figure 3. The elements for the transmitting and receiving antenna are short dipole antennas with simple omni-directional radiation pattern and vertically polarized. A ray-tracing
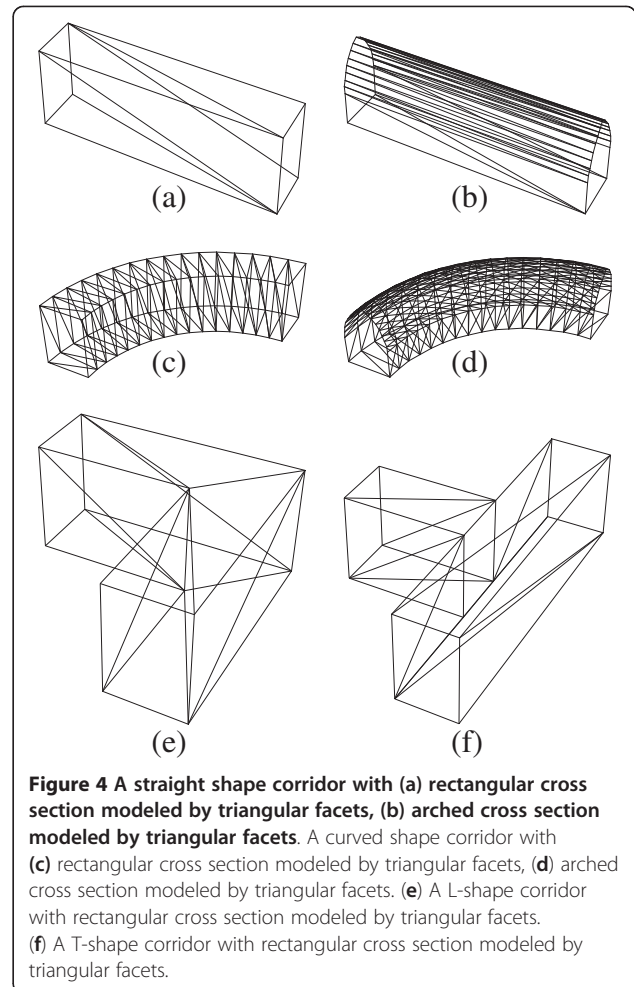
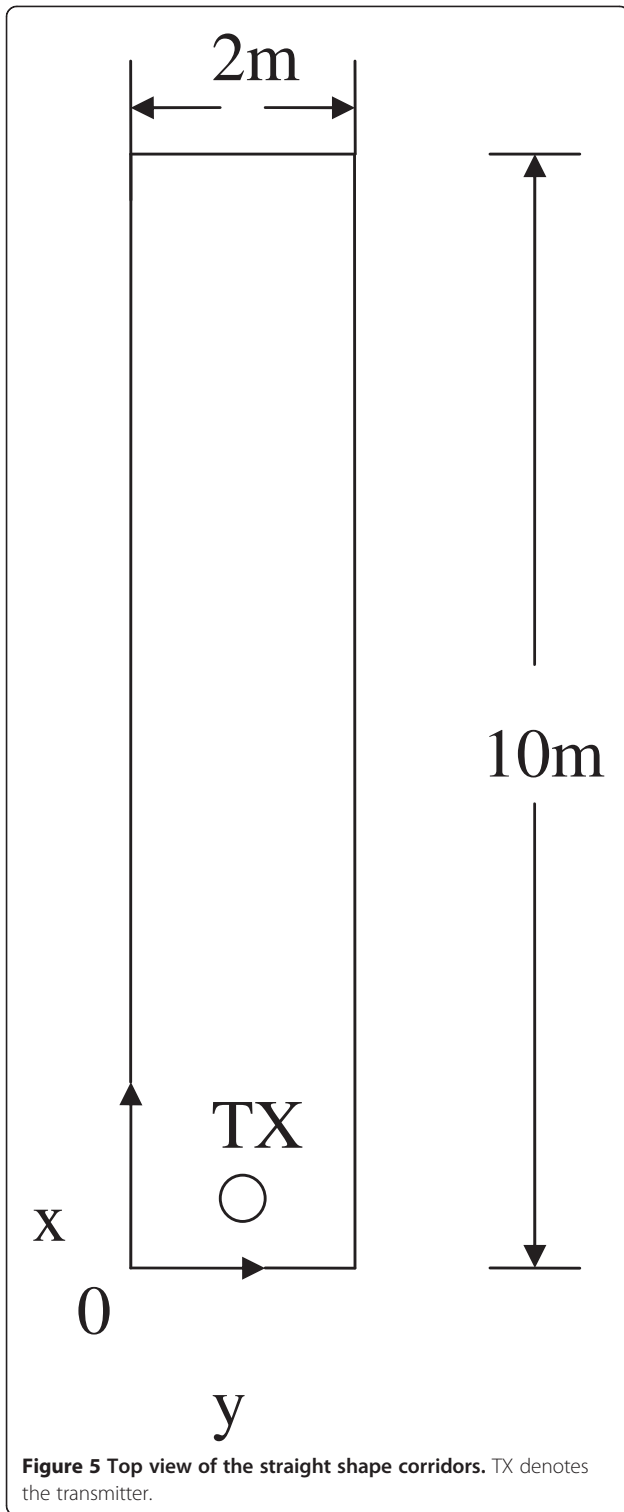**Figure 3 Geometry of a transmitting and receiving antenna arrays.**



**Figure 4 A straight shape corridor with (a) rectangular cross section modeled by triangular facets, (b) arched cross section modeled by triangular facets**. A curved shape corridor with (**c**) rectangular cross section modeled by triangular facets, (**d**) arched cross section modeled by triangular facets. (**e**) A L-shape corridor with rectangular cross section modeled by triangular facets. (**f**) A T-shape corridor with rectangular cross section modeled by triangular facets.

technique is developed to calculate the channel frequency response from 59.5 to 60.5 GHz with a frequency interval of 5 MHz. i.e., 201 frequency components are used. For example, the relative permittivity and conductivity of the other different materials can be referred in [37-40]. The dielectric constant and conductivity of the concrete materials are shown in Table 1. The maximum number of bounces setting beforehand for these corridors is 10, and the convergence is confirmed.

This article intends to compare the channel characteristics of six different corridors, which are composed of triangular facets is shown in Figures 4a–f. The straight corridors with rectangular and arched section are, respectively, shown in Figure 4a,b. The curved shape corridors with rectangular and arched cross sections are, respectively, shown in Figure 4c,d. The L-shape corridor with rectangular cross section is given in Figure 4e, whereas the T-shape corridor with rectangular cross section is given in Figure 4f. The top view of the straight shape corridors is plotted in Figure 5. Note that the top
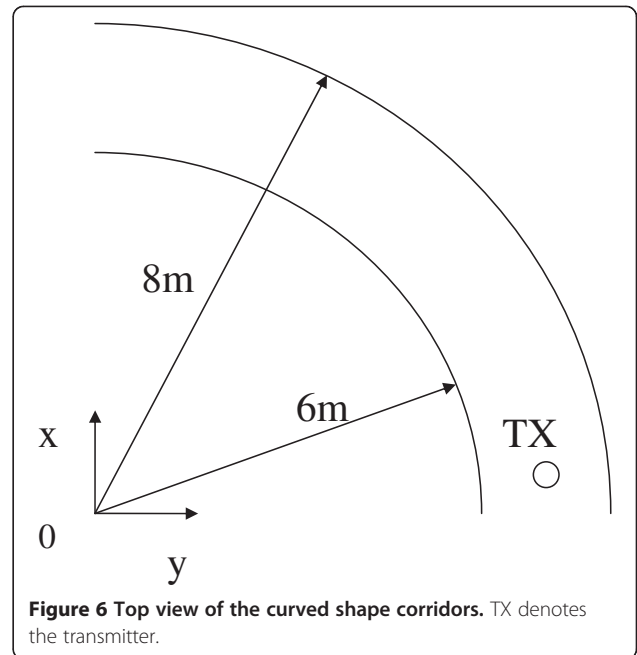
views of Figure 4a,b are the same. Figure 6 shows the top view of curved shape corridors. The top view of the L-shape corridor is shown in Figure 7. Figure 8 shows the top view of the T-shape corridor. The cross sections of all corridors are 2-m wide and 3-m high. The lengths of straight shape corridors with rectangular and arched section are 10 m. The inner and outer radius of the curved shape corridors with rectangular and arched cross section are, respectively, 6 and 8 m. 30−cm thick walls and ceilings of the concrete are used for these corridors.

The transmitting and receiving antennas in these six different corridors are both short dipole antennas and vertically polarized. The positions of transmitting antenna (TX) for these corridors are shown in Figures 4, 5, 6, and 7 with the fixed height of 1.5 m. There are 270 receiving points for each corridor. The locations of receiving antennas in these six different corridors are distributed uniformly with a fixed height of 1 m. The distance between two adjacent receiving points is 0.25 m.

A three-dimensional SBR/image technique has been presented in this article. This technique is used to

**Table 1 Dielectric properties of concrete materials measured at 60 GHz**

| Materials | Relative permittivity | | | |
|---|---|---|---|---|
| | Real | Imaginary | Conductivity | Tan loss |
| | $\varepsilon'$ | $\varepsilon''$ | $\sigma$ | $Tan(\delta)$ |
| Concrete | 6.4954 | 0.4284 | 1.43E+00 | 6.60E−02 |

**Figure 5 Top view of the straight shape corridors.** TX denotes the transmitter.



**Figure 6 Top view of the curved shape corridors.** TX denotes the transmitter.

The RMS delay spread $\tau_{\mathrm{RMS}}$ is defined as follows [41]:

$$\tau_{\mathrm{RMS}} = \sqrt{\frac{\sum_{n=1}^{N} \tau_n{}^2 |a_n|^2}{G} - \left(\frac{\sum_{n=1}^{N} \tau_n |a_n|^2}{G}\right)^2},$$

(10)

where $G = \sum_{n=1}^{N} |a_n|^2$ is the total multipath gain.



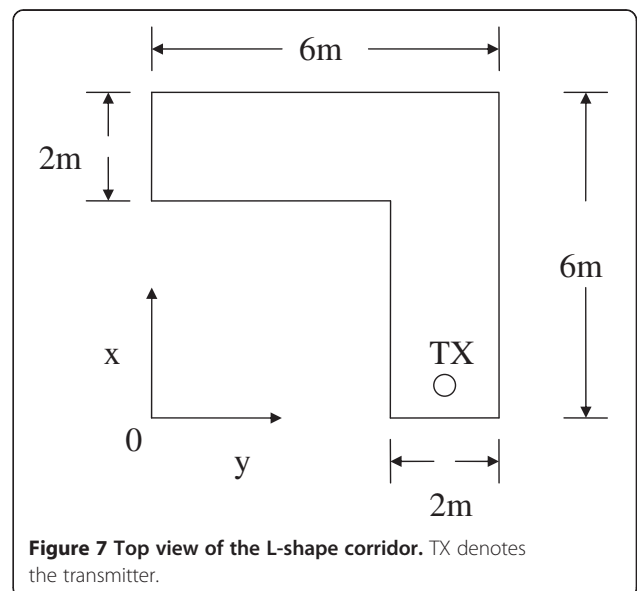**Figure 7 Top view of the L-shape corridor.** TX denotes the transmitter.

calculate the WLAN channel impulse response for each location of the receiver. Based on the channel impulse response, the number of multipath components, the root mean square (RMS) delay spread $\tau_{\mathrm{RMS}}$, and the mean excess delay $\tau_{\mathrm{MED}}$ are computed.
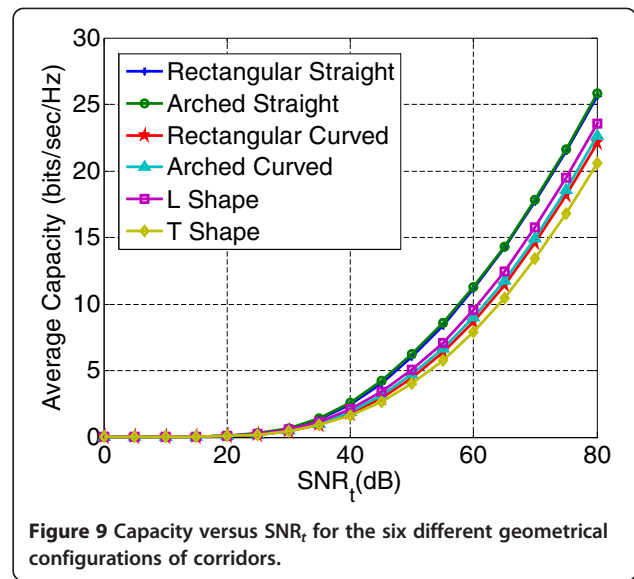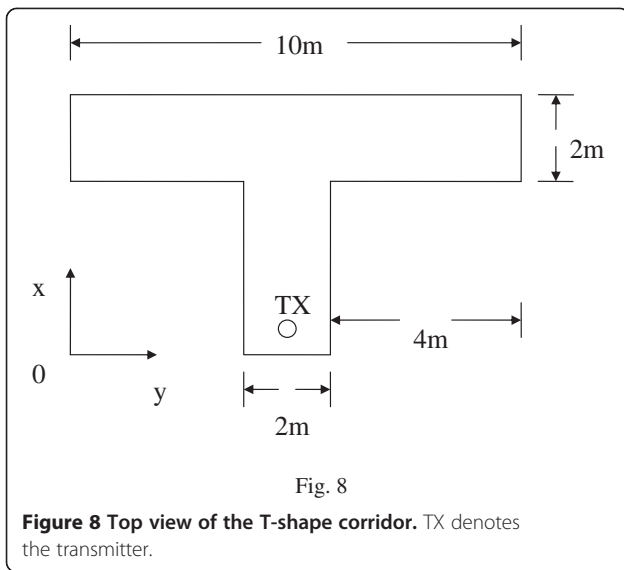
Fig. 8

**Figure 8 Top view of the T-shape corridor.** TX denotes the transmitter.



**Figure 9 Capacity versus SNR$_t$ for the six different geometrical configurations of corridors.**

The MED, $\overline{\tau}$, is defined as follows [42-53]:

$$\overline{\tau} = \frac{\sum_{n=1}^{N} \tau_n |a_n|^2}{G} \tag{11}$$

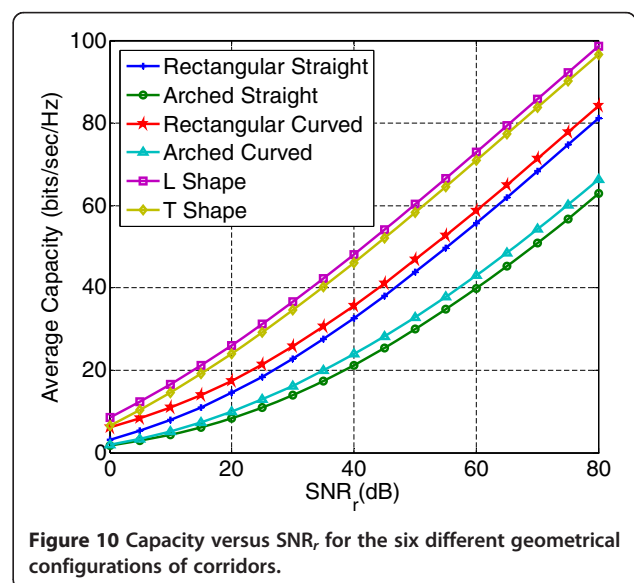By Equations (10) and (11), we can obtain the RMS delay spreads and MED.

In this article, the capacity versus SNR$_t$ for these six corridors is calculated. Here, channel capacity is the average information rate over the ensemble of channel realizations. There are 270 receiving points for each corridor. In truth, the capacity in Equation (7) can be calculated by equal transmitting powers in these six different corridors. SNR$_t$ is the ratio of total transmitting power to noise power for 270 receiving points. As a result, the channel realizations for various receiving locations are combined into one ensemble with 270 samples.

In other words, we have calculated the SNR$_t$ in all receiving positions. Capacity using that SNR$_t$ is computed in Figure 9. The capacity versus SNR$_t$ plots for these six corridors are given in Figure 9. Here, SNR$_t$ is defined as the ratio of the average transmitting power to the noise power. The results show that the capacity for arched straight corridors is larger than those shape corridors. It is due to the fact that the arched straight corridors can minimize the fading and reduce the multipath effects. Numerical results show that the rectangular straight and arched straight corridors are maximum capacity. The straight and arched straight corridors are to calculate the received power for these corridors. The results show that the received power for rectangular straight and arched straight corridors is larger than those shape corridors. It is due to the fact that the rectangular straight and arched straight corridors can maximize the received power and minimize the fading and reduce the multipath effects. In

other words, rectangular straight and arched straight corridors are only LoS positions. It is due to the fact that the rectangular straight and arched straight corridors can maximize the received power, resulting in more than the capacity.

MIMO can dramatically increase channel capacity not only due to the beamforming gain and diversity gain, but also MIMO spatial multiplexing technique makes full use of multipath fading. Furthermore, a channel matrix is vitally interrelated to calculate the received power. As a result, the capacity can be increased substantially in straight shape corridors with rectangular and arched sections.

Let us consider the capacity performance for six corridors. The capacity versus SNR$_r$ plots for these six corridors are given in Figure 10. Here, SNR$_r$ is defined as the



**Figure 10 Capacity versus SNR$_r$ for the six different geometrical configurations of corridors.**

**Table 2 Parameters of multipath channel for the six different geometrical configurations of corridors**

| Shapes | $\tau_{MED}$ (ns) | | $\tau_{RMS}$ (ns) | |
|---|---|---|---|---|
| | Mean | Standard deviation | Mean | Standard deviation |
| Rectangular straight | 0.83 | 0.35 | 1.65 | 0.54 |
| Arched straight | 0.97 | 0.45 | 1.46 | 0.42 |
| Rectangular curved | 1.68 | 1.59 | 1.90 | 0.54 |
| Arched curved | 1.76 | 1.51 | 1.47 | 0.49 |
| L-shape | 4.48 | 5.06 | 2.59 | 0.73 |
| T-shape | 5.60 | 5.37 | 2.47 | 0.78 |

ratio of the average power to the noise power at the front end of the receiver. The results show that the capacity for T-shape corridor and L-shape corridor is greater than the other corridors since the multipath effect caused by the back wall for light-of-sight (LOS) cases is severe and the number of receiving points of non-light-of-sight (NLOS) cases are greater than others.

Table 2 shows $\tau_{RMS}$ and $\tau_{MED}$ for these six corridors. There are two parameters, including RMS delay spread, MED. The RMS delay spread is the square root of the second central moment of the power delay profile. It is also found that the mean RMS delay spreads for the arched cross section corridors are smaller than those for the rectangular cross section corridors regardless of the shapes. This situation can be explained by the fact that the multipath effect for the arched cross section corridors is less severe than those for the rectangular cross section corridors. Besides, we can see that the RMS delay spreads for the straight shape corridor with rectangular cross section are almost the same as those for the curved shape corridor with rectangular cross section. Similar results are found for the arched cross section corridors. This is due to the reason that most waves inside the curved corridors arrived simultaneously owing to the curved geometry and this results in small RMS delay spreads. Finally, we can find that the RMS delay spreads for the T-shape corridor and L-shape corridor are greater than the other corridors since the multipath effect caused by the back wall for LOS cases is severe and the number of receiving points of NLOS cases is greater than others. The MEDs are the rectangular straight, arched straight, rectangular curved, and arched curved corridors are smaller than those for the

L-shape and T-shape corridors. This situation can be explained by the fact that the multipath effect for the rectangular straight, arched straight, rectangular curved, and arched curved corridors are less severe than those for the L-shape and T-shape corridors. The MED of rectangular straight is 0.83 ns and increases about 18% to 0.98 ns for arched straight corridor. It is also seen that the MED of rectangular curved is 1.69 ns and increases about 5% to 1.77 ns for arched curved corridor. The MED of rectangular straight is 0.83 ns and increases about 4.77 to 5.6 ns for T-shape corridor. Finally, we can find that the MEDs for the T-shape and L-shape corridors are greater than the other corridors since the multipath effect caused by the back wall for LOS cases is severe and the number of receiving points of NLOS cases are greater than others.

The $\tau_{RMS}$ and $\tau_{MED}$ for these six corridors with 10 and 50 reflections are, respectively, shown in Table 3. The mean RMS delay spread for the T-shape with 10 reflections is 2.47 ns and increases about 1.6% to 2.51 ns for the T-shape with 50 reflections. It is also seen that the MED for the L-shape with 10 reflections is 4.48 ns and increases about 0.6% to 4.51 ns for the L-shape with 50 reflections. Therefore, the maximum number of bounces setting beforehand for these corridors is 10, and the convergence is confirmed.

## 4. Conclusions

Comparison is made of $4 \times 4$ MIMO–WLAN communication characteristics for corridors of different shapes and cross sections. The frequency dependence on materials utilized in the structure on the indoor channel is accounted for in the channel simulation. The MED and

**Table 3 The $\tau_{RMS}$ and $\tau_{MED}$ for these six corridors with 10 and 50 reflections**

| Shapes | $\tau_{MED}$ (ns) | | $\tau_{RMS}$ (ns) | |
|---|---|---|---|---|
| | Mean (10 reflections) | Mean (50 reflections) | Mean (10 reflections) | Mean (50 reflections) |
| Rectangular straight | 0.83 | 0.845 | 1.65 | 1.668 |
| Arched straight | 0.97 | 0.989 | 1.46 | 1.475 |
| Rectangular curved | 1.68 | 1.702 | 1.90 | 1.928 |
| Arched curved | 1.76 | 1.785 | 1.47 | 1.491 |
| L-shape | 4.48 | 4.516 | 2.59 | 2.629 |
| T-shape | 5.60 | 5.645 | 2.47 | 2.515 |

RMS delay spread for six different channels are computed by the SBR/image method and inverse Fourier transform. Numerical results are given for the capacity varying with channel shapes and cross sections. Furthermore, we find that the capacity for the rectangular straight and arched straight corridors is greater than corridors of other shapes. The capacity for T-shape corridor is smallest among all shapes. The RMS delay spread for arched straight corridor is smaller than those corridors regardless of the shapes. It is found that the RMS delay spread for the T-shape corridor is the largest. Besides, the RMS delay spread for arched cross section corridors are less than those for rectangular cross section corridors regardless of the shapes.

## Competing interests

The authors declare that they have no competing interests.

## Author details

[1]Department of Electrical Engineering, Tamkang University, Tamsui Dist, New Taipei City, Taiwan. [2]Department of Information Technology and Mobile Communication, Taipei College of Maritime Technology, Danshui Town, New Taipei City, Taiwan.

## References

1. A Maltsev, R Maslennikov, A Sevastyanov, A Khoryaev, A Lomayev, Experimental investigations of 60 GHz WLAN systems in office environment. IEEE J. Sel. Areas Commun. **27**(8), 1488–1499 (2009)
2. PFM Smulders, AG Wagemans, Wideband indoor radio propagation measurements at 58 GHz. IEE Electron. Lett. **28**(13), 1270–1271 (1992)
3. N Moraitis, P Constantinou, Measurements and characterization of wideband indoor radio channel at 60 GHz. IEEE Trans. Wirel. Commun. **5**(4), 880–889 (2006)
4. J Lee, HL Bertoni, Coupling at cross, T and L junctions in tunnels and urban street canyons. IEEE Trans. Antennas Propagat. **15**(5), 926–935 (2003)
5. A Goldsmith, SA Jafar, N Jindal, Capacity limits of MIMO channels. IEEE J. Sel. Areas Commun. **21**(5), 684–702 (2003)
6. SL Loyka, Channel capacity of MIMO architecture using the exponential correlation matrix. IEEE Commun. Lett. **5**(9), 369–371 (2001)
7. KI Ziri-Castro, WG Scanlon, NE Evans, Prediction of variation in MIMO channel capacity for the populated indoor environment using a radar cross-section-based pedestrian model. IEEE Trans. Wirel. Commun. **4**(3), 1186–1194 (2005)
8. Z Tang, AS Mohan, Experimental investigation of indoor MIMO Ricean channel capacity. IEEE Antennas Wirel. Propagat. Lett. **4**, 55–58 (2005)
9. DW Browne, M Manteghi, MP Fitz, Y Rahmat-Samii, Experiments with compact antenna arrays for MIMO radio communications. IEEE Trans. Antennas Propagat. **54**(11), 3239–3250 (2006)
10. J-M Molina-Garcia-Pardo, J-V Rodriguez, L Juan-Llacer, Polarized indoor MIMO channel measurements at 2.45 GHz. IEEE Trans. Antennas Propagat **56**(12), 3818–3828 (2008)
11. P Smulders, Exploiting the 60 GHz band for local wireless multimedia access: prospects and future directions. IEEE Commun. Mag. **40**(1), 140–147 (2002)
12. IEEE Standard for Information Technology, Telecommunications and information exchange between systems—Local and metropolitan area networks—Specific requirements—Part 11: Wireless LAN Medium Access Control (MAC) and Physical Layer (PHY) Specifications. IEEE Standard **802**, 11 (2007)
13. AH Wong, MJ Neve, KW Sowerby, Antenna selection and deployment strategies for indoor wireless communication systems. IET Commun. **1**(4), 732–738 (2007)
14. DCK Lee, MJ Neve, KW Sowerby, The impact of structural shielding on the performance of wireless systems in a single-floor office building. IEEE Trans. Wirel. Commun. **6**(5), 1787–1795 (2007)
15. G Liang, HL Bertoni, A new approach to 3-D ray tracing for propagation prediction in cities. IEEE Trans. Antennas Propagat. **46**, 853–863 (1998)
16. Y Zhang, Ultra-wide bandwidth channel analysis in time domain using 3-D ray tracing, in *High Frequency Postgraduate Student Colloquium of IEEE* (, Manchester, England, 2004), pp. 6–7
17. S Woo, H Yang, M Park, B Kang, Phase-included simulation of UWB channel. IEICE Trans. Commun. **E88-B**, 1294–1297 (2005)
18. SH Chen, SK Jeng, An SBR/Image approach for indoor radio propagation in a corridor. IEICE Trans. Electron **E78-C**, 1058–1062 (1995)
19. SH Chen, SK Jeng, SBR image approach for radio wave propagation in tunnels with and without traffic. IEEE Trans. Veh. Technol **45**, 570–578 (1996)
20. Z Yan, H Yang, A Akram, P Clive, UWB on-body radio channel modeling using ray theory and subband FDTD method. IEEE Trans. Microw. Theory Tech. **54**(2, part. 2), 1827–1835 (2006)
21. Y Zhang, AK Brown, Complex multipath effects in UWB communication channels. IEE Proc. Commun. **153**(1), 120–126 (2006)
22. PC Richardson, X Weidong, S Wayne, Modeling of ultra-wideband channels within vehicles. IEEE J. Sel. Areas Commun. **24**(4), 906–912 (2006)
23. PF Driessen, GJ Foschini, On the capacity formula for multiple input-multiple output wireless channels: a geometric interpretation. IEEE Trans. Commun. **47**(2), 173–176 (1999)
24. F Tila, PR Shepherd, SR Pennock, Theoretical capacity evaluation of indoor micro- and macro-MIMO systems at 5 GHz using site specific ray tracing. Electron. Lett. **39**(5), 471–472 (2004)
25. SH Oh, NH Myung, MIMO channel estimation method using ray-tracing propagation model. Electron. Lett. **40**(21), 1350–1352 (2004)
26. L Susana, R-A Alberto, RP Torres, Indoor MIMO channel modeling by Rigorous GO/UTD-based ray tracing. IEEE Trans. Veh. Technol. **57**(2), 680–692 (2008)
27. S-H Chen, S-K Jeng, An SBR/image approach for radio wave propagation in indoor environments with metallic furniture. IEEE Trans. Antennas Propagat. **45**(1), 98–106 (1997)
28. CA Balanis, *Advanced Engineering Electromagnetics* (Wiley, New York, 1989)
29. MF Iskander, Y Zhengqing, Propagation prediction models for wireless communication systems. IEEE Trans. Microw. Theory Tech. **50**(3), 662–673 (2002)
30. I Oppermann, M Hamalainen, J Iinatti, *UWB Theory and Applications* (Wiley, New York, 2004)
31. EW Kamen, BS Heck, *Fundamentals of Signals and Systems Using the Web and Matlab* (Prentice-Hall (Upper Saddle River, NJ, 2000)
32. WQ Malik, CJ Stevens, DJ Edwards, Spatio-temporal ultrawideband indoor propagation modeling by reduced complexity geometric optics. IEET Commun. **1**(4), 751–759 (2007)
33. G Strang, *Linear Algebra and its Applications* (Harcourt Brace Jovanovich, San Diego, 1988)
34. Z Xu, S Sfar, RS Blum, Analysis of MIMO systems with receive antenna selection in spatially correlated Rayleigh fading channels. IEEE Trans. Veh. Technol. **58**(1), 251–262 (2009)
35. WJ Chang, JH Tarng, SY Peng, Frequency-space-polarization on UWB MIMO performance for body area network applications. IEEE Antennas Wirel. Propagat. Lett. **7**, 577–580 (2008)
36. JF Valenzuela Valdés, MA García-Fernández, AM Martinez-Gonzalez, DA Sanchez-Hernandez, The influence of efficiency on receive diversity and MIMO capacity for Rayleigh-fading channels. IEEE Trans. Antennas Propagat. **56**(5), 1444–1450 (2008)
37. LM Correia, PO Francês, Estimation of materials characteristics from power measurements at 60 GHz, in *International Symposium on Personal, Indoor and Mobile Radio Communications, vol. 2* (Den Haag, Netherlands, 1994), pp. 510–513
38. Y Pinhasi, A Yahalom, S Petnev, Propagation of ultra wide-band signals in lossy dispersive media, in *IEEE International Conference on Microwaves, Communications, Antennas and Electronic Systems* (COMCAS, Tel-Aviv, Israel, 2008), pp. 1–10
39. P Vainikainen, *On the properties of dielectric materials in mobile communications environments, in COST 2100 TD(10)12097* (, Bologna, Italy, 2010)
40. Y Lostanlen, Y Corre, Y Louet, Y Le Helloco, S Collonge, Comparison of measurements and simulations in indoor environments for wireless local networks at 60 GHz, in *IEEE 55th Vehicular Technology Conference, vol. 1* (Birmingham, Alabama, USA, 2002), pp. 389–393

41. M Gabriella, D Benedetto, G Giancola, *Understanding Ultra Wide Band Radio Fundamentals* (Prentice Hall, Upper Saddle River, NJ, 2004)
42. TS Rappaport, *Wireless Communications: Principles and Practice, 2nd edn. (Upper* (Prentice Hall PTR, Upper Saddle River, NJ, 2002)
43. MH Ho, CC Chiu, SH Liao, Optimization of Channel Capacity for MIMO Smart Antenna Using Particle Swarm Optimizer. IET Communications **6**(16), 2645–2563 (2012)
44. CC Chiu, CH Chen, SH Liao, KC Chen, Bit Error Rate Reduction by Smart UWB Antenna Array in Indoor Wireless Communication. Journal of Applied Science and Engineering **15**(2), 139–148 (2012)
45. MH Ho, CC Chiu, SH Liao, Bit Error Rate Reduction for Circular Ultrawideband Antenna by Dynamic Differential Evolution. International Journal of RF and Microwave Computer-Aided Engineering **22**(2), 260–271 (2012)
46. CC Chiu, CH Chen, SH Liao, TC Tu, Ultra-wideband Outdoor Communication Characteristics with and without Traffic. EURASIP Journal on Wireless Communications and Networking **92** (2012)
47. SH Liao, MH Ho, CC Chiu, CH Lin, Optimal Relay Antenna Location in Indoor Environment Using Particle Swarm Optimizer and Genetic Algorithm. Wireless Personal Communications **62**(3), 599–615 (2012)
48. CC Chiu, YT Kao, SH Liao, YF Huang, 'UWB Communication Characteristics for Different Materials and Shapes of the Stairs. Journal of Communications **6**(8), 628–632 (2011)
49. SH Liao, HP Chen, CC Chiu, CL Liu, Channel Capacities of Indoor MIMO-UWB Transmission for Different Material Partitions. Tamkang Journal of Science and Engineering **14**(no.1), 49–63 (2011)
50. SH Liao, MH Ho, CC Chiu, Bit Error Rate Reduction for Multiusers by Smart UWB Antenna Array. Progress In Electromagnetic Research C **16**, 85–98 (2010). PIER C 16
51. MH Ho, SH Liao, CC Chiu, A Novel Smart UWB Antenna Array Design by PSO. Progress In Electromagnetic Research C **15. PIER C 15**, 103–115 (2010)
52. MH Ho, SH Liao, CC Chiu, UWB Communication Characteristics for Different Distribution of People and Various Materials of Walls. Tamkang Journal of Science and Engineering **13**(3), 315–326 (2010)
53. CL Liu, CC Chiu, SH Liao, YS Chen, Impact of Metallic Furniture on UWB Channel Statistical Characteristics. Tamkang Journal of Science and Engineering **12**(3), 271–278 (2009)